Study of Common Quantification Methods of Amide Proton Transfer Magnetic Resonance Imaging for Ischemic Stroke Detection

Lee Sze Foo, B.S, [a], James R Larkin, PhD, [b], Brad A. Sutherland, PhD, [c, d], Kevin J. Ray, DPhil, [b], Wun-She Yap, PhD, [e], Yan Chai Hum, PhD, [a], Khin Wee Lai, PhD, [f], Hanani Abdul Manan, PhD, [g], Nicola R. Sibson, PhD, [b], Yee Kai Tee, DPhil, [a*].

[a] Department of Mechatronics and Biomedical Engineering, Lee Kong Chian Faculty of Engineering and Science, Universiti Tunku Abdul Rahman, Malaysia.

[b] Department of Oncology, Cancer Research UK and Medical Research Council Oxford Institute for Radiation Oncology, University of Oxford, UK.

[c] Tasmanian School of Medicine, College of Health and Medicine, University of Tasmania, Australia.

[d] Acute Stroke Programme, Radcliffe Department of Medicine, University of Oxford, United Kingdom.

[e] Department of Electrical and Electronic Engineering, Lee Kong Chian Faculty of Engineering and Science, Universiti Tunku Abdul Rahman, Malaysia.

[f] University of Malaya, Faculty of Engineering, Department of Biomedical Engineering, Jalan Universiti, Kuala Lumpur, 50603, Malaysia.

[g] Department of Radiology, Universiti Kebangsaan Malaysia Medical Centre, Malaysia.

Running Title: Quantification methods of APT MRI for ischemic stroke detection

Word Count: 5141

[*]**Correspondence to**:

Yee Kai Tee

Universiti Tunku Abdul Rahman,
Jalan Sungai Long,
Bandar Sungai Long
Cheras 43000, Kajang,
Selangor, Malaysia.

Email: teeyeekai@gmail.com

ABSTRACT

Purpose: To assess the correlation and differences between common amide proton transfer (APT) quantification methods in ischemic stroke diagnosis.

Methods: Five APT quantification methods, including asymmetry analysis and its variants as well as two Lorentzian model-based methods, were applied on data acquired from six rats that underwent middle cerebral artery occlusion scanned at 9.4 T. Diffusion and perfusion weighted images, and water relaxation time maps were also acquired to study the relationship of these conventional imaging modalities with the different APT quantification methods.

Results: The APT ischemic area estimates had varying sizes (Jaccard index: $0.544 \leq J \leq 0.971$) and had varying correlations in their distributions (Pearson correlation coefficient: $0.104 \leq r \leq 0.995$), revealing discrepancies in the quantified ischemic areas. The Lorentzian methods produced the highest CNRs ($1.427 \leq \text{CNR} \leq 2.002$), but generated APT ischemic areas that were comparable in size to CBF deficit area; asymmetry analysis and its variants produced APT ischemic areas that were smaller than CBF but larger than ADC deficit areas although having lower CNRs ($0.561 \leq \text{CNR} \leq 1.083$).

Conclusion: There is a need to further investigate the accuracy and correlation of each quantification method with the pathophysiology using a larger scale multi-imaging modality and multi-time point clinical study. Future studies should include the MTR_{asym} results alongside the findings of their study, in order to facilitate the comparison of results between different centers and also the published literature.

KEYWORDS

Amide proton transfer (APT); Magnetic Resonance Imaging (MRI); Chemical Exchange Saturation Transfer (CEST); Ischemic Stroke.

1 Introduction

During ischemic stroke, two major zones of injury occur – the infarct core and the penumbra (1). The infarct core contains tissue that is irreversibly damaged upon ischemia and cannot be salvaged. In contrast, the penumbra contains tissue surrounding the core that is at risk of infarction, but which may still be salvaged if timely reperfusion is performed. The aim of acute stroke therapy is to recover the ischemic penumbra using recanalization strategies to minimize the final area of infarction.

The current imaging technique for identifying the ischemic penumbra is the spatial mismatch between diffusion-weighted imaging (DWI) and perfusion-weighted imaging (PWI) (2,3). However, the mismatch area always overestimates the penumbra and falsely includes regions of benign oligemia – a region of tissue that recovers spontaneously even without therapeutic intervention (4). This limitation highlights the critical need for a new imaging approach that is able to more accurately identify the ischemic penumbra to optimize treatment outcome.

Chemical exchange saturation transfer (CEST) is a magnetic resonance imaging (MRI) technique in which contrast originates from exogenous or endogenous exchangeable protons or molecules (5,6). Through analyzing the CEST effects of various endogenous exchangeable protons, many studies have reported the potential of CEST MRI to be used for ischemic stroke imaging (7–12). In particular, amide proton transfer (APT) – a variant of CEST MRI relating to the labile amide protons of endogenous proteins and/or peptides resonating at 3.5 ppm downfield from water resonance, has been shown to be pH-sensitive owing to the base-catalyzed chemical exchange process between amide and water protons (13–16). Since pH reduction is the last stage before cell infarction (17), it has been hypothesized that the ischemic lesion may be better identified via pH-sensitive imaging instead of the mismatch between DWI and PWI. This concept aligns with the pH-sensitive nature of APT imaging, allowing for its potential to serve as a non-invasive pH-weighted imaging technique, complementing perfusion and diffusion MRI for ischemic stroke diagnosis. To date, many publications on the potential use of APT imaging for stroke diagnosis (14,18,19), disease progression (20), and treatment monitoring (21,22) have been reported. However, in these studies, different experimental parameters and quantification methods were used for analysis. The lack of standardization in these experiments complicates comparison of results between the research centers.

A previous study highlighted the discrepancies between different centers with regards to changes in CEST signal due to ischemia, with certain CEST effects reported to increase, decrease, or remain unchanged upon ischemia, depending on the time, acquisition parameters and quantification methods used (23). For APT, in terms of the general trend of signal changes in ischemic lesions, the majority of studies have reported a decrease in APT

effect in ischemic infarction. Despite this, a few conflicting studies have reported no changes in APT signal within ischemic tissue, depending on the experimental parameters. One study found the contrast between ischemic and normal tissue to diminish at a certain saturation power (24), whilst a more recent study observed no visual or significant statistical differences regardless of low or high saturation power when imaged at the very high field strength of 21.1 T (25). In publications on the delineation of the different zones of ischemic injury, some studies have reported that APT is able to differentiate between the ischemic core, penumbra, and oligemia (7,9), whilst one study reported no significant differences between the three regions (26).

There are many possible explanations for the discrepancies observed between the research centers. One of the possible sources of inconsistency is the use of different quantification methods. In the current literature, different quantification methods have been used for analysis, including the more commonly used model-free methods, or more complex quantitative model-based methods. The use of different quantification methods makes it difficult to compare these existing APT experiments in a meaningful manner.

To facilitate the clinical translation of APT imaging, this study aims to analyze commonly used APT quantification methods for acute ischemic stroke in order to assess the differences and correlations between the quantification methods. CEST data from six rats that underwent a commonly used model of stroke were retrospectively analyzed using five APT quantification methods. The ischemic areas estimated by each method were compared, and the relative quantified APT effects in the ischemic and contralateral regions were analyzed. In addition, the advantages and limitations of the different quantification methods were briefly discussed in order to provide an overview on the suitability of the quantification methods for clinical ischemic stroke imaging and recommendations to ease the comparison of findings between research centers for future investigations.

2 Methods and Materials

2.1 APT Quantification Methods

CEST data are collected by measuring the water signal amplitude of the subject when applying radio frequency (RF) pulse over a range of saturation frequencies, ω. The measured signal as a function of these saturation frequencies is commonly known as the z-spectrum. APT involves quantifying and analyzing the CEST effect at the resonant frequency of amide protons, around 3.5 ppm in the z-spectrum.

Many quantification methods for APT effect analysis have been proposed. Supporting Table S1 in Supplementary Materials summarizes a list of APT quantification methods used for ischemic stroke imaging including the advantages and limitations of each method. In this study, only some of the most commonly used APT quantification methods were used for analysis (underlined in Supporting Table S1 and defined in the Supplementary Materials), i.e. magnetization transfer ratio asymmetry (MTR_{asym}) (13), water relaxation time T_1-normalized MTR_{asym} (27–29), apparent exchange-dependent relaxation (AREX) (12,30,31), Lorentzian difference analysis (LDA) (12,25,26,32) and multi-Lorentzian fitting (27,33,34). Other methods were excluded due to unsuitable experimental parameters as this was a retrospective analysis.

2.2 Animal Stroke Model

The animal experiments were approved by the UK Home Office (Animals [Scientific Procedures] Act 1986) and conducted in accordance with the University of Oxford Policy on the Use of Animals in Scientific Research and the ARRIVE guidelines. Middle cerebral artery occlusion (MCAO) was induced in six Sprague Dawley rats (referred to as Animals 1 – 6) via intraluminal filament method by advancing a filament (Doccol, USA) up the internal carotid artery to block the MCA (35). The filament remained in place while imaging was performed.

2.3 Magnetic Resonance Imaging

All MR images of the animals were acquired using a 9.4 T field strength scanner (Agilent, CA, USA), including T_1, T_2, CEST, DWI, and PWI. All images were of 0.5 x 0.5 x 1 mm^3 spatial resolution, acquired using spin echo EPI with a 64 x 64 matrix size. Briefly, T_1-weighted images were acquired with repetition time (TR) of 10000 ms, echo time (TE) of 27.16 ms, and nine inversion times (TI) ranging from 13.14 – 8000 ms. T_2-weighted images were obtained using TR = 5000 ms and ten TEs from 30 – 160 ms. DWIs were obtained at *b*-values of 0 and 1000 s/mm^2. For PWI, a multiphase pseudo-continuous arterial spin labeling (MP-PCASL) was implemented at 8 RF phase offsets ranging from 0º to 315º with TR = 4000 ms and TE = 28.68 ms. The label plane was placed in the neck, perpendicular to the carotid arteries. The label duration was 1.4 s and comprised of a series of Hanning-shaped pulses each 600 µs long, separated by 600 µs. The post label delay was 0.55 s. Reference images for coil sensitivity and baseline signal intensity were acquired by omitting labelling pulses. PWI acquisition time was 1.48 min. For CEST MRI, multi-slice images were obtained at frequency offsets -4.1, -3.8, -3.5, -3.2, -2.9, -2.6, -2.3, -2, -1.7, -1.5, -1.2, -0.9, -0.6, -0.3, 0, 0.3, 0.6, 0.9, 1.2, 1.5, 1.6, 1.7, 1.8, 1.9, 2, 2.1, 2.4, 2.7, 2.9, 3.1, 3.2, 3.3, 3.4, 3.5, 3.6, 3.7, 3.8, 3.9, 4.1, 5, 7, 9.7, 13.5, 19, 26, 37, 51, 72, 100, and ±300 ppm (used as unsaturated images). Saturation was

performed using 50 primary and 5 secondary Gaussian pulses of 20 ms pulse duration, 50 % duty cycle, and 184º flip angle, equivalent to an average power of 0.547 μT. The acquisition time of each CEST experiment was 8.67 min.

2.4 Data Processing and Analysis

Apparent diffusion coefficient (ADC) images were calculated as $\mathrm{ADC} = -\frac{1}{b_2 - b_1}\ln\left({S_{b_2}}/{S_{b_1}}\right)$ using DWIs at b = 0 and 1000 s/mm^2. From the ADC maps, K-means clustering was used to automatically define the ischemic lesions and produce a binary lesion mask (9,11,18,36), with number of clusters, k = 2 and K-means++ algorithm for center initialization seeding. A contralateral mask was then manually drawn opposite to and having the same size as the ischemic lesion mask.

T_1 maps were generated via least-squares fitting of the measured signals, S, as a function of inversion times, TI: $S = \left|a + c \cdot \exp\left(-{\mathrm{TI}}/{\mathrm{T_1}}\right)\right|$, where a and c are constants. Similarly, T_2 maps were obtained by fitting to a mono-exponential function of echo times, TE: $S = S_0 \exp\left(-{\mathrm{TE}}/{\mathrm{T_2}}\right)$. Cerebral blood flow (CBF) maps were calculated using a model-based fitting approach fully described elsewhere (37), but in brief supervoxel clustering was used to define regions with similar phase offsets in the raw multiphase data, these supervoxels were used to obtain high-SNR phase maps which were used to inform a Bayesian multiphase fitting approach to give calibrated CBF maps.

The B_0 field inhomogeneity of the CEST data was corrected voxel-wise via single-Lorentzian water pool fitting at frequency offsets assumed to have no other CEST effects besides direct saturation (32): within ±1.2 ppm and above/below ±6.0 ppm. The inhomogeneity-corrected CEST data were then processed using the five APT quantification methods: MTR_{asym}, T_1-normalized MTR_{asym}, AREX, LDA, and multi-Lorentzian fitting. The amide proton resonance was taken as the average of 3.5 ± 0.1 ppm, and opposite reference offsets were average of -3.5 ± 0.3 ppm. MTR_{asym}, T_1-normalized MTR_{asym} and AREX were calculated using the opposite offset signals as reference. In LDA, the frequency offsets used for the single-pool Lorentzian lineshape fitting were those assumed to have no other CEST effects except direct water saturation, similar to the offsets used for B_0 correction. For multi-Lorentzian fitting, the number of pools modelled was 6 in total, including water at 0 ppm, MT at 0 ppm, amide at 3.5 ppm, NOE at -3.5 ppm, amine at 2 ppm, and NOE at -1.6 ppm. For Lorentzian lineshape fitting in LDA and multi-Lorentzian fitting, the Lorentzian lineshape model was first fitted to the averaged z-spectra of the brain to obtain its fitted parameters. Then, voxel-wise fitting was

performed, allowing the fitting parameters to vary within 30% of the fitted parameters of the averaged z-spectra.

To enable composite voxel-wise analysis across all six animals, relative quantified T_1, T_2, and APT effects were calculated by normalizing the quantified APT effect of the ischemic and contralateral tissue, by the absolute averaged signal in the contralateral tissue, that is, $\mathrm{r}S_{\mathrm{ischem}} = S_{\mathrm{ischem}}/|\mathrm{mean}(S_{\mathrm{contra}})|$ and $\mathrm{r}S_{\mathrm{contra}} = S_{\mathrm{contra}}/|\mathrm{mean}(S_{\mathrm{contra}})|$, where S_{ischem} refers to the signal in the ADC ischemic region and S_{contra} is the signal in the contralateral region. A two-tailed paired t-test at 5% significance level was used to test for significant differences between the relative values in ischemic and contralateral regions. The coefficient of variation (CV) of the MR images was calculated using the composite relative values of the contralateral tissue of all six animals: $\mathrm{CV} = \mathrm{SD}(\mathrm{r}S_{\mathrm{contra}})/\mathrm{mean}(\mathrm{r}S_{\mathrm{contra}})$, where SD refers to standard deviation. In addition, the contrast-to-noise ratio (CNR) was also calculated using the composite relative values as $\mathrm{CNR} = |\mathrm{mean}(\mathrm{r}S_{\mathrm{contra}}) - \mathrm{mean}(\mathrm{r}S_{\mathrm{ischem}})|/\mathrm{SD}(\mathrm{r}S_{\mathrm{contra}})$.

To compare the ischemic lesion predictions of the T_1, T_2, CBF, and APT images with the ADC defined ischemic lesion, the same K-means clustering settings as the ADC processing was used to automatically segment the ischemic region from each of the generated images (9,11,18,36). In addition, for the APT images, the Jaccard index (*J)* – a measure of intersection between two binary images, was calculated to quantify the differences between areas of ischemic lesion predictions of the five quantification methods. The mathematical representation of the Jaccard index is written as:

$$J(A,B) = \frac{\text{Area of Overlap}}{\text{Area of Union}} = \frac{|A \cap B|}{|A \cup B|}. \quad (1)$$

The Jaccard index between the APT ischemic area of each quantification method pair was separately calculated for every animal. Besides that, the Jaccard index between the APT ischemic area of each quantification method and the ADC ischemic area was also quantified for every animal. Kruskal-Wallis test was then used to compare the quantified Jaccard indices for significant differences.

For comparing the APT signal variations, Mann-Whitney U test was used to test for significant differences between the relative quantified effects within the APT ischemic areas using the different methods. Lastly, Pearson's correlation coefficient, *r*, between the relative quantified APT effects in the ADC ischemic lesion, $\mathrm{r}S_{\mathrm{ischem}}$ was calculated to evaluate the correlations between distributions of the quantification methods.

3 Results

Figure 1 shows the ADC, T_1, T_2 and APT images of four representative animals (Animals 1 – 4) subject to MCAO. The MR images of Animals 5 and 6 can be found in Supplementary Materials (Supporting Figure S1). The final row of Figure 1 shows the collective relative quantified values of all six animals (Animals 1 – 6) of each MR image. The composite relative quantified values of the MR images are summarized in Table 1.

As shown in column 1 of Figure 1, it was observed that all the ADC maps showed a substantial deficit in the ischemic regions. In all six animals, the ADC deficit area had a composite relative ADC of 0.743 ± 0.066 while the contralateral tissue had relative ADC of 1.000 ± 0.066, corresponding to CV of 0.066 and CNR of 3.878. From the ADC maps, K-means clustering was used to define the ischemic lesion masks (red) and corresponding contralateral tissue masks (blue) were manually drawn for each animal, shown overlaid on the ADC images.

The T_1 and T_2 maps of the animals are shown in the second and third column of Figure 1 respectively. T_1 was found to be hyperintense in the ischemic regions (composite relative T_1 = 1.159 ± 0.091) and significantly different from the contralateral tissue (composite relative T_1 = 1.000 ± 0.074), resulting in CV = 0.074 and CNR = 2.143. Conversely, there was no significant difference between the T_2 values of ischemic and contralateral areas, although collectively, T_2 was lower in the ischemic areas (ischemic area: composite relative T_2 = 0.984 ± 0.079; contralateral area: composite relative T_2 = 1.000 ± 0.160), similar to the results reported by Sun et al. (36). The T_2 relative values produced a low CNR of 0.100 and CV of 0.160.

The last five columns in Figure 1 show the APT images generated using the different quantification methods. The quantified APT effect in ischemic tissue was consistently hypointense compared to non-ischemic tissue, observed in the APT images of all of the quantification methods, and in the composite relative values (Table 1), consistent with previous reports (13,38). Paired t-test at 5% significance level revealed the relative quantified APT effects in the ADC ischemic regions to be significantly different from those in the contralateral areas, indicating that all five methods were able to distinguish the ischemic area from the contralateral non-ischemic tissue.

However, although all methods were able to differentiate between ischemic and non-ischemic tissue, for a given animal, it could be observed that the APT images generated by different methods had different patterns in the signal variations, describing different variations of heterogeneity. The APT images also had hypointense areas of varying sizes.

Of the five quantification methods, LDA produced the highest CNR of 2.002 and lowest CV of 0.143, followed by multi-Lorentzian fitting with CNR of 1.427 and CV of 0.152. Among the

model-free methods, MTR_{asym} produced the highest CNR of 1.083 and lowest CV of 0.590, followed by T_1-normalized MTR_{asym} with CNR of 0.655 and CV of 0.609. Lastly, AREX produced the lowest CNR of 0.561 and highest CV of 0.623.

To compare between the APT ischemic area predictions of the different quantification methods, K-means clustering was used to segment the ischemic areas. Figure 2 shows the predicted ischemic areas of the APT images of the four representative animals (Animals 1 – 4), as well as the ADC and CBF maps. The predicted ischemic areas of Animals 5 and 6 can be found in Supplementary Materials (Supporting Figure S2). For each animal, the top row of images shows the ADC and APT images of different quantification methods. It was observed that the ischemic area estimated by each quantification method coincided well with the ADC lesion. However, the APT ischemic areas had noticeable variation in sizes. The binary masks of the ischemic areas of each APT quantification method were summed to produce a map of overlapping APT ischemic lesions, shown in the last column. From this overlap map, it was observed that the APT-predicted lesions had a high overlap within the ADC lesions and fewer overlap beyond the ADC deficit area.

The CBF/APT/ADC mismatch images are shown in the bottom row for each animal in Figure 2. In these mismatch images, it was observed that the CBF deficit areas were larger than that of ADC for all animals. For APT ischemic areas, it was found that MTR_{asym}, T_1-normalized MTR_{asym}, and AREX produced APT ischemic lesion predictions that were larger than ADC lesion but smaller than CBF lesions. In contrast, the Lorentzian model-based methods – LDA and multi-Lorentzian fitting produced ischemic areas that were equal to or even larger than the CBF lesions for certain animals.

The differences between the ischemic masks produced from each quantification method were compared by calculating Jaccard indices where $J = 1$ represents a complete overlap and $J = 0$ indicates no overlapping. Figure 3 shows the comparison of a representative animal (Animal 1). In the figure, each plot corresponds to the comparison of the ischemic area of a pair of APT quantification methods. The APT ischemic lesion estimates had large areas of overlap, but described lesions of varying sizes, evident in the variation in Jaccard indices ($0.551 \leq J \leq 0.928$).

The Jaccard indices of all six animals are shown in Table 2. The averaged Jaccard index comparing between the APT and ADC lesions ranged from 0.503 – 0.567, where a Kruskal-Wallis test indicated the Jaccard indices to be insignificantly different with $P = 0.9167$, implying all the methods were able to pick up the ADC lesions. In contrast, the averaged Jaccard indices comparing between each pair of quantification methods, covered a wider range of 0.544 – 0.971, with a Kruskal-Wallis test revealing the indices to be significantly different with

$P = 1.016 \times 10^{-5}$, highlighting the variations in the quantified APT lesion areas. From the indices, it was observed that the ischemic areas of the model-free methods – MTR_{asym}, T_1-normalized MTR_{asym}, and AREX shared the highest similarities ($J \geq 0.895 \pm 0.051$). This was expected as the model-free methods are based on MTR_{asym} but with slight modifications or corrections.

Apart from the differences in APT ischemic area sizes, the APT lesions were also observed to have different signal variations from one another. Mann-Whitney U test was used to test for significant differences between the relative quantified APT effects within the APT lesions using the different methods. The test was repeated for all six animals. The calculated *P*-values for each of the animals can be found in Supporting Table S2 of Supplementary Materials. In general, it was found that the relative quantified effects using the different methods were significantly different from one another ($P < 0.05$) in large majority of the animals, with the exceptions of the pairs: T_1-normalized MTR_{asym} and AREX, as well as LDA and multi-Lorentzian fitting having no significant differences from one another.

To analyze the correlation between the distributions of the different APT quantification methods within the ADC lesions, the Pearson's correlation coefficient of the collective relative quantified APT effects were calculated, as shown in Figure 4. It was found that the model-free methods showed very strong correlation with one another, with $0.957 \leq r \leq 0.995$. For the Lorentzian lineshape model-based methods, LDA had moderate correlation with multi-Lorentzian fitting ($r = 0.555$), weak correlation with MTR_{asym} ($r = 0.282$), and very weak correlations with T_1-normalized MTR_{asym} and AREX ($r = 0.173, 0.104$); multi-Lorentzian fitting had moderate correlations with MTR_{asym} ($r = 0.401$), and weak correlations with T_1-normalized MTR_{asym} and AREX ($r = 0.347, 0.311$).

4 Discussion

To date, many quantification methods have been proposed for APT ischemic stroke experiments (Supporting Table S1). However, there is currently no standardized method for quantifying the APT effect in ischemic stroke, resulting in the comparison of results generated by different research groups becoming a non-trivial task. This present study sought to analyze the commonly used APT quantification methods for ischemic stroke imaging in order to assess the spatial differences and correlations of the ischemic lesion estimates of the different methods.

From Figure 1, in terms of the conventional MR images, the T_1 maps were able to distinguish between the ischemic and contralateral regions, while T_2 was not able to pick up on any early stroke changes as the composite relative T_2 did not produce significant differences between

the tissues. This was in line with past publications in that T_1 was found to be consistently hyperintense in ischemic tissue, while T_2, although having overall changes in the signal, was not found to have significant statistical differences in early stroke imaging (36,39). The ischemic areas of the relaxation maps can be found in Supporting Figure S3 of Supplementary Materials.

Comparing between the APT images, it was found that ischemic lesion areas predicted by the different APT quantification methods were different from one another, both in terms of lesion sizes (Figure 2 and Figure 3) and signal variations (Supporting Table S2 and Figure 4). This inconsistency may also be observed in previous publications that investigated the use of more than one APT quantification method. In those studies, the presented APT images of different quantification methods also had seemingly different signal patterns, in both animal models (18,27) and ischemic stroke patients (9,12,14,26).

In this retrospective study, it was not possible to explain the differences in the different APT images or relate them to the underlying physiological changes of the tissue. In order to further verify the efficiency and accuracy of each quantification method for acute stroke diagnosis, a multi-parametric imaging and multi-time point investigation similar to the studies by Harston et al. (7), Heo et al. (9), and Msayib et al. (12) is needed to identify the sizes, heterogeneity, and changes in the core, penumbra, and oligemia across multiple time points. These three studies have shown APT imaging to have the potential for identifying the ischemic penumbra from the infarct core and benign oligemia (7,9,12), which is currently lacking in conventional imaging techniques.

Two of these studies have investigated the use of different quantification methods in order to determine the most optimal method for ischemic stroke imaging at multiple time points (9,12). In the study by Msayib et al. (12), the quantitative APT ratio (APTR*) via Bloch-McConnell model fitting (40) was found to be the most optimal method. However, the computational time of APTR* analysis is beyond clinically feasible time for acute stroke diagnosis (41,42). Unless some form of compromise is used, such as continuous approximation (14,43), or if the processing time of the full Bloch-McConnell model fitting can be improved substantially, APTR* is unlikely to be an ideal method for acute stroke application.

In addition, in the two mentioned studies, the main metrics used to determine the most optimal method were CV, CNR, or similar metrics for quantifying spatial variability and contrast between ischemic and non-ischemic tissue (9,12). Although these metrics would indeed determine the method that would provide the highest contrast between the ischemic and non-ischemic tissue and the least spatial variability, this may not necessarily reflect the actual pathophysiology of the brain. As the results of this present study show, although LDA and

multi-Lorentzian fitting produced the highest CNR and lowest CV among the tested methods, suggesting the Lorentzian model-based methods to be more optimal than the model-free methods, both Lorentzian model-based methods estimated ischemic areas that were comparable in size to the CBF lesions (Figure 2). These findings differed from previous studies that reported APT predicted ischemic lesions to be smaller than PWI deficits (9,18,19) and do not support the hypothesis that the APT hypointense area should be smaller than the PWI deficit area as it delineates between the ischemic penumbra and benign oligemia. Thus, CNR and CV calculations may be a good measure of the spatial variations of the brain but are less meaningful if they do not correlate with the physiology. Therefore, further work is needed to investigate more clinically viable quantification methods for their accuracy in describing the physiology of the ischemic cerebral environment, using a similar study design to the three mentioned studies (7,9,12).

In this study, two Lorentzian model-based methods – LDA and multi-Lorentzian fitting were used. It should be noted that the use of LDA is more suited for low power saturations where MT effect is negligible and single-pool Lorentzian fitting of the direct water saturation is sufficient (32). For higher power experiments, single-pool Lorentzian fitting for LDA may cause fitting errors due to the presence of MT effect and broader saturation effect, resulting in non-Lorentzian lineshape. When multi-Lorentzian fitting is used for high power data, the fitted amide pool may contain contaminations from nearby amines which have multiple components, broad peak width, and non-Lorentzian lineshape due to coalescence effect (44). Nevertheless, we found the direct water saturation and CEST effects to approximate Lorentzian lineshapes well in this study because a low power saturation (0.547 μT) was used. The average z-spectra of the ischemic and contralateral areas of the animals can be found in Supporting Figure S4.

From the correlations of the APT effects quantified by the different methods in Figure 4, it was observed that among the model-free methods, T_1-normalized MTR_{asym} and AREX shared stronger correlation with one another compared with MTR_{asym}. While T_1-normalized MTR_{asym} and AREX both compensate for T_1, only AREX corrects for the MT effect. Thus, the stronger correlation between T_1-normalized MTR_{asym} and AREX compared with T_1-normalized MTR_{asym} and MTR_{asym} suggests that it is not necessary to correct for MT, but necessary to compensate for T_1 in acute stroke. This finding was in agreement with previous studies that reported nearly no changes in MT (45), but significant changes in T_1 in acute stroke (36,39).

It is also worth noting that previous studies have found that APT effect does not linearly depend on T_1. Instead, the relationship between the two is dependent on the CEST acquisition parameters (46,47). As such, depending on the experimental parameters, normalizing the APT effect by T_1 may cause an overcorrection and reduced APT contrast. This was found to

be the case in brain tumour imaging, where the water proton concentration and T_1 shared a linear correlation, which may cause an overcorrection when normalizing APT effect by T_1 (48). The same study has not been conducted in ischemic stroke; a future study investigating this to improve detection of the penumbra will be worthwhile but is beyond the scope of the current work.

To compare between the ischemic area predictions of each quantification method, K-means clustering was used to automatically segment the quantified APT effects into ischemic and non-ischemic tissue in this study. This approach was used because it is difficult to manually differentiate between the gray matter (GM) and white matter (WM) in rat brain as the brain volume is small and the image resolution is not high; this differs from the clinical gold standard of having experienced radiologists to draw the ischemic region of the interest (ROI). The segmented clusters of the quantified APT effect in each of the six animals using the k-means clustering can be found in Supporting Figure S5 of Supplementary Materials; it was able to segment the quantified APT effects into two clusters – the hypointense ischemic tissue and the non-ischemic tissue.

So far, in terms of the general trend of APT signal change during ischemia, although the majority of studies have reported a decrease in APT signal, there have been a few conflicting reports compared to the majority (24,25). These inconsistent findings may be the result of differing image acquisition parameters, the physiology of the disease itself, or the quantification method used during analysis, as demonstrated in this study. It is not currently possible to directly compare the results and determine the true source of the discrepancies, as there are many variables between the experiments. However, since APT imaging of stroke is still in its development stages and further work is still required to determine the optimal APT quantification method, it may still be too early to standardize APT experimental parameters and quantification methods.

As such, to enable the comparison of results from studies conducted by different centers, this paper presents three recommendations. Particularly, authors should report (whenever possible): (1) the overall trend of change of relative MTR_{asym}(~3.5 ppm) in ischemic tissue (significantly decreased, increased, or no significant changes), (2) the CEST acquisition parameters used, and (3) the ROI(s) in which the APT effects were investigated, e.g. DWI deficit, PWI deficit, follow-up FLAIR, etc. We make these recommendations as it would help different research groups compare the changes of APT signal during ischemic stroke within the defined ROI, when imaged using certain acquisition parameters. Relative MTR_{asym} is suggested in this case as it has a historical dataset in the literature, being the most commonly

used method in ischemic stroke experiments (Supporting Table S1), and is easy to calculate, report and interpret, with minimum conflicting variation between centers.

To aid in the comparison of existing reports on APT imaging of stroke, Supporting Table S3 and Supporting Table S4 in Supplementary Materials summarize reports in the current literature on the changes of MTR_{asym}(~3.5 ppm) during ischemia and the corresponding acquisition parameters used as well as the ROIs in which the APT effects were investigated. Albeit not a direct comparison, this would simplify the comparison of results between centers as it would exclude the quantification method as the potential source of any discrepancies. This summary of MTR_{asym}(~3.5 ppm) results and experimental parameters may also provide useful information for future CEST experiments as it presents the list of experimental parameters that are known to produce positive results and are useful for ischemic stroke imaging, as well as experimental parameters that should be avoided.

5 Conclusion

The five tested APT quantification methods were all able to distinguish the ischemic region as hypointense compared to non-ischemic tissue. However, the estimated ischemic areas of the methods varied in sizes and heterogeneity within the tissue. In the current literature, there have been a few inconsistencies on the trends of APT signal during ischemia. To fully investigate the accuracy and correlation of each quantification method on its description of ischemic pathophysiology, a larger scale multi-imaging modality and multi-time point clinical study is needed. As further work is still needed before optimizing and standardizing experimental and quantification methods for APT imaging in ischemic stroke, it is proposed that future studies should report the results of MTR_{asym} alongside other APT quantification methods used in the study, in order to enable comparison between results of different centers and the published literature.

Acknowledgements

YKT was supported by National Cancer Council Malaysia (MAKNA) Cancer Research Award 2018 as well as UTAR Research Fund (project number: IPSR/RMC/UTARRF/2018-C1/T04 & IPSR/RMC/UTARRF/2020-C1/T02), and would like to gratefully acknowledge the support of NVIDIA Corporation with the donation of a Quadro P6000 GPU for this research. JRL and NRS were supported by Cancer Research UK (grant number: C5255/A1593). BAS was supported by the National Health and Medical Research Council of Australia (APP1137776) and the Rebecca J Cooper Foundation. BAS and NRS were supported by a Wellcome Trust

Institutional Strategic Support Fund grant. KJR was funded by a Medical Research Council studentship (MC_ST_U13080) and supplementary award (MR/K501256/1).

Disclosures

The authors have no competing interests to declare.

References

1. Zhou Z, Lu J, Liu WW, et al. Advances in stroke pharmacology. Pharmacol. Ther. 2018 doi: 10.1016/j.pharmthera.2018.05.012.

2. Wheeler HM, Mlynash M, Inoue M, et al. Early diffusion-weighted imaging and perfusion-weighted imaging lesion volumes forecast final infarct size in DEFUSE 2. Stroke 2013 doi: 10.1161/STROKEAHA.111.000135.

3. Bernhardt J, Zorowitz RD, Becker KJ, et al. Advances in stroke 2017. Stroke 2018 doi: 10.1161/STROKEAHA.118.021380.

4. Leigh R, Knutsson L, Zhou J, van Zijl PCM. Imaging the physiological evolution of the ischemic penumbra in acute ischemic stroke. J. Cereb. Blood Flow Metab. 2018;38:1500–1516 doi: 10.1177/0271678X17700913.

5. Ward KM, Balaban RS. Determination of pH using water protons and chemical exchange dependent saturation transfer (CEST). Magn. Reson. Med. 2000;44:799–802 doi: 10.1002/1522-2594(200011)44:5<799::AID-MRM18>3.0.CO;2-S.

6. Ward KM, Aletras AH, Balaban RS. A New Class of Contrast Agents for MRI Based on Proton Chemical Exchange Dependent Saturation Transfer (CEST). J. Magn. Reson. 2000;143:79–87 doi: 10.1006/jmre.1999.1956.

7. Harston GWJ, Tee YK, Blockley N, et al. Identifying the ischaemic penumbra using pH-weighted magnetic resonance imaging. Brain 2015;138:36–42 doi: 10.1093/brain/awu374.

8. Jin T, Wang P, Jin T, Kim SG, Kim SG. Enhancing sensitivity of pH-weighted MRI with combination of amide and guanidyl CEST. Neuroimage 2017;157:341–350 doi: 10.1016/j.neuroimage.2017.06.007.

9. Heo HY, Zhang Y, Burton TM, et al. Improving the detection sensitivity of pH-weighted amide proton transfer MRI in acute stroke patients using extrapolated semisolid magnetization transfer reference signals. Magn. Reson. Med. 2017;78:871–880 doi: 10.1002/mrm.26799.

10. Zhou IY, Lu D, Ji Y, et al. Determination of multipool contributions to endogenous amide proton transfer effects in global ischemia with high spectral resolution in vivo chemical exchange saturation transfer MRI. Magn. Reson. Med. 2018;81:645–652 doi: 10.1002/mrm.27385.

11. Wang E, Wu Y, Cheung JS, et al. Mapping tissue pH in an experimental model of acute stroke – Determination of graded regional tissue pH changes with non-invasive quantitative amide proton transfer MRI. Neuroimage 2019;191:610–617 doi: 10.1016/j.neuroimage.2019.02.022.

12. Msayib Y, Harston GWJ, Tee YK, et al. Quantitative CEST imaging of amide proton transfer in acute ischaemic stroke. NeuroImage Clin. 2019;23:101833 doi: 10.1016/j.nicl.2019.101833.

13. Zhou J, Payen J-F, Wilson DA, Traystman RJ, van Zijl PCM. Using the amide proton signals of intracellular proteins and peptides to detect pH effects in MRI. Nat. Med. 2003;9:1085–90 doi: 10.1038/nm907.

14. Tee YK, Harston GWJ, Blockley N, et al. Comparing different analysis methods for quantifying the MRI amide proton transfer (APT) effect in hyperacute stroke patients. NMR Biomed. 2014;27:1019–1029 doi: 10.1002/nbm.3147.

15. Ray KJ, Larkin JR, Tee YK, et al. Determination of an optimally sensitive and specific chemical exchange saturation transfer MRI quantification metric in relevant biological phantoms. NMR Biomed. 2016;29:1624–1633 doi: 10.1002/nbm.3614.

16. Ray KJ, Simard MA, Larkin JR, et al. Tumor pH and protein concentration contribute to the signal of amide proton transfer magnetic resonance imaging. Cancer Res. 2019 doi: 10.1158/0008-5472.CAN-18-2168.

17. Hossman KA. Pathophysiological basis of translational stroke research. Folia Neuropathol. 2009.

18. Guo Y, Zhou IY, Chan ST, et al. pH-sensitive MRI demarcates graded tissue acidification during acute stroke — pH specificity enhancement with magnetization transfer and relaxation-normalized amide proton transfer (APT) MRI. Neuroimage 2016 doi: 10.1016/j.neuroimage.2016.07.025.

19. Sun PZ. Fast correction of B0 field inhomogeneity for pH-specific magnetization transfer and relaxation normalized amide proton transfer imaging of acute ischemic stroke without Z-spectrum. Magn. Reson. Med. 2019;0:1–10 doi: 10.1002/mrm.28040.

20. Lin G, Zhuang C, Shen Z, et al. APT weighted MRI as an effective imaging protocol to predict clinical outcome after acute ischemic stroke. Front. Neurol. 2018;9:1–9 doi: 10.3389/fneur.2018.00901.

21. Yu L, Chen Y, Chen M, et al. Amide proton transfer MRI signal as a surrogate biomarker of ischemic stroke recovery in patients with supportive treatment. Front. Neurol. 2019;10 doi: 10.3389/fneur.2019.00104.

22. Park JE, Jung SC, Kim HS, et al. Amide proton transfer–weighted MRI can detect tissue acidosis and monitor recovery in a transient middle cerebral artery occlusion model compared with a permanent occlusion model in rats. Eur. Radiol. 2019 doi: 10.1007/s00330-018-5964-3.

23. Tee YK, Abidin B, Khrapitchev A, et al. CEST and NOE signals in ischemic stroke at 9.4T evaluated using a Lorentzian multi-pool analysis: a drop, an increase or no change? In: Proc Int Soc Magn Reson Med. ; 2017.

24. Dai Z, Ji J, Xiao G, et al. Magnetization transfer prepared gradient echo MRI for CEST imaging. PLoS One 2014;9 doi: 10.1371/journal.pone.0112219.

25. Roussel T, Rosenberg JT, Grant SC, Frydman L. Brain investigations of rodent disease models by chemical exchange saturation transfer at 21.1 T. NMR Biomed. 2018;31:1–13 doi: 10.1002/nbm.3995.

26. Tietze A, Blicher J, Mikkelsen IK, et al. Assessment of ischemic penumbra in patients with hyperacute stroke using amide proton transfer (APT) chemical exchange saturation transfer (CEST) MRI. NMR Biomed. 2014;27:163–174 doi: 10.1002/nbm.3048.

27. Wu Y, Zhou IY, Lu D, et al. pH-sensitive amide proton transfer effect dominates the magnetization transfer asymmetry contrast during acute ischemia—quantification of multipool contribution to in vivo CEST MRI. Magn. Reson. Med. 2018;79:1602–1608 doi: 10.1002/mrm.26829.

28. Zu Z, Afzal A, Li H, Xie J, Gore JC. Spin-lock imaging of early tissue pH changes in ischemic rat brain. NMR Biomed. 2018 doi: 10.1002/nbm.3893.

29. Sun PZ, Cheung JS, Wang E, Lo EH. Association between pH-weighted endogenous amide proton chemical exchange saturation transfer MRI and tissue lactic acidosis during acute ischemic stroke. J. Cereb. Blood Flow Metab. 2011;31:1743–1750 doi: 10.1038/jcbfm.2011.23.

30. Zaiss M, Xu J, Goerke S, et al. Inverse Z-spectrum analysis for spillover-, MT-, and T1-corrected steady-state pulsed CEST-MRI - application to pH-weighted MRI of acute stroke. NMR Biomed. 2014;27:240–252 doi: 10.1002/nbm.3054.

31. Li H, Zu Z, Zaiss M, et al. Imaging of amide proton transfer and nuclear Overhauser enhancement in ischemic stroke with corrections for competing effects. NMR Biomed. 2015 doi: 10.1002/nbm.3243.

32. Jones CK, Polders D, Hua J, et al. In vivo three-dimensional whole-brain pulsed steady-state chemical exchange saturation transfer at 7 T. Magn. Reson. Med. 2012 doi: 10.1002/mrm.23141.

33. Zaiß M, Schmitt B, Bachert P. Quantitative separation of CEST effect from magnetization transfer and spillover effects by Lorentzian-line-fit analysis of z-spectra. J. Magn. Reson. 2011;211:149–155 doi: 10.1016/j.jmr.2011.05.001.

34. Zhang XY, Wang F, Afzal A, et al. A new NOE-mediated MT signal at around -1.6 ppm for detecting ischemic stroke in rat brain. Magn. Reson. Imaging 2016;34:1100–1106 doi: 10.1016/j.mri.2016.05.002.

35. Sutherland BA, Buchan AM. Alteplase treatment does not increase brain injury after mechanical middle cerebral artery occlusion in the rat. J. Cereb. Blood Flow Metab. 2013 doi: 10.1038/jcbfm.2013.148.

36. Sun PZ. Demonstration of magnetization transfer and relaxation normalized pH-specific pulse-amide proton transfer imaging in an animal model of acute stroke. Magn. Reson. Med. 2020 doi: 10.1002/mrm.28223.

37. Larkin JR, Simard MA, Khrapitchev AA, et al. Quantitative blood flow measurement in rat brain with multiphase arterial spin labelling magnetic resonance imaging. J. Cereb. Blood Flow Metab. 2019 doi: 10.1177/0271678X18756218.

38. Zhou J, Heo HY, Knutsson L, van Zijl PCM, Jiang S. APT-weighted MRI: Techniques, current neuro applications, and challenging issues. J. Magn. Reson. Imaging 2019;50:347–364 doi: 10.1002/jmri.26645.

39. Lu D, Jiang Y, Ji Y, et al. Evaluation of diffusion kurtosis imaging of stroke lesion with hemodynamic and metabolic MRI in a rodent model of acute stroke. Am. J. Roentgenol. 2018 doi: 10.2214/AJR.17.19134.

40. Chappell MA, Donahue MJ, Tee YK, et al. Quantitative Bayesian model-based analysis of amide proton transfer MRI. Magn. Reson. Med. 2013;70:556–567 doi: 10.1002/mrm.24474.

41. Foo LS, Yap W-S, Tee YK. Determination of computationally efficient multi-pool model fitting approach for pulsed chemical exchange saturation transfer MRI. In: 2019 8th International Conference on Bioinformatics and Biomedical Science. Beijing: ACM; 2019. doi: 10.1145/3369166.3369175.

42. Foo LS, Yap WS, Hum YC, Manan HA, Tee YK. Analysis of model-based and model-free CEST effect quantification methods for different medical applications. J. Magn. Reson. 2020;310 doi: 10.1016/j.jmr.2019.106648.

43. Tee YK, Khrapitchev AA, Sibson NR, Payne SJ, Chappell MA. Evaluating the use of a continuous approximation for model-based quantification of pulsed chemical exchange saturation transfer (CEST). J. Magn. Reson. 2012;222:88–95 doi: 10.1016/j.jmr.2012.07.003.

44. Zhang XY, Wang F, Li H, et al. Accuracy in the quantification of chemical exchange saturation transfer (CEST) and relayed nuclear Overhauser enhancement (rNOE) saturation transfer effects. NMR Biomed. 2017;30 doi: 10.1002/nbm.3716.

45. Zhou IY, Lu D, Ji Y, et al. Determination of multipool contributions to endogenous amide proton transfer effects in global ischemia with high spectral resolution in vivo chemical exchange saturation transfer MRI. Magn. Reson. Med. 2019;81:645–652 doi: 10.1002/mrm.27385.

46. Heo HY, Lee DH, Zhang Y, et al. Insight into the quantitative metrics of chemical exchange saturation transfer (CEST) imaging. Magn. Reson. Med. 2017;77:1853–1865 doi: 10.1002/mrm.26264.

47. Zu Z. Towards the complex dependence of MTRasym on T1w in amide proton transfer (APT) imaging. NMR Biomed. 2018 doi: 10.1002/nbm.3934.

48. Lee DH, Heo HY, Zhang K, et al. Quantitative assessment of the effects of water proton concentration and water T 1 changes on amide proton transfer (APT) and nuclear overhauser enhancement (NOE) MRI: The origin of the APT imaging signal in brain tumor. Magn. Reson. Med. 2017;77:855–863 doi: 10.1002/mrm.26131.

List of Tables

Table 1. Relative quantified values of the MRIs within the ADC ischemic lesion and contralateral normal region of the six animals undergoing MCAO. * indicates a significant difference at 5% significance level ($P < 0.05$).

Images	Contralateral Area	Ischemic Area	Difference (Ischemic – Contralateral)	*P*-value	CV	CNR
ADC	1.000 ± 0.066	0.743 ± 0.066	-0.257*	0	0.066	3.878
T_1	1.000 ± 0.074	1.159 ± 0.091	0.159*	1.362×10^{-99}	0.074	2.143
T_2	1.000 ± 0.160	0.984 ± 0.079	-0.016	0.051	0.160	0.100
MTR_{asym}	-1.000 ± 0.590	-1.639 ± 0.697	-0.639*	9.342×10^{-42}	0.590	1.083
T_1-normalized MTR_{asym}	-1.000 ± 0.609	-1.399 ± 0.627	-0.399*	1.485×10^{-20}	0.609	0.655
AREX	-1.000 ± 0.623	-1.349 ± 0.625	-0.349*	4.326×10^{-16}	0.623	0.561
LDA	1.000 ± 0.143	0.715 ± 0.168	-0.285*	1.286×10^{-97}	0.143	2.002
Multi-Lorentzian fitting	1.000 ± 0.152	0.783 ± 0.144	-0.217*	1.592×10^{-77}	0.152	1.427

Table 2. Jaccard indices between the ischemic lesion areas of all six animals estimated using the different quantification methods, shown as mean ± standard deviation.

Quantification Method	MTRasym	T1-normalized MTRasym	AREX	LDA	Multi-Lorentzian Fitting
MTRasym	**0.567 ± 0.171**	0.905 ± 0.036	0.895 ± 0.051	0.576 ± 0.090	0.591 ± 0.198
T1-normalized MTRasym		**0.516 ± 0.154**	0.971 ± 0.027	0.545 ± 0.090	0.563 ± 0.210
AREX			**0.517 ± 0.170**	0.544 ± 0.087	0.556 ± 0.212
LDA				**0.503 ± 0.110**	0.691 ± 0.156
Multi-Lorentzian Fitting					**0.549 ± 0.108**

Figure Captions

Figure 1. MR images of the four representative rats (Animals 1 – 4) subject to MCAO shown in the first four rows respectively. The first column shows the ADC images ($\mu m^2/ms$), overlaid with the ischemic (red) and contralateral (blue) regions of interest (ROI). The second and third column show the T_1 (s) and T_2 maps (ms); subsequent columns correspond to APT images generated using different quantification methods: MTR_{asym}, T_1-normalized MTR_{asym}, AREX, LDA, and multi-Lorentzian fitting (%). The final row shows the relative quantified APT effects of all six animals (n = 6) within the contralateral and ischemic tissues of each quantification method; * indicates a significant difference between the two tissues at 5% significance level.

Figure 2. ADC ($\mu m^2/ms$), CBF (mL/100g/min), and APT (%) images of four representative animals (Animals 1 – 4), with the respective ischemic areas outlined: ADC – white, APT – blue and CBF – green. For every animal, the ADC and APT images are shown in the top row along with the binary ischemic area overlaps of all five APT methods in the last column, where higher intensity indicates a higher overlap. The bottom row shows the CBF map as well as the CBF/APT/ADC lesion mismatches of every APT quantification method; the display priority in the mismatch plots is white > blue > green.

Figure 3. Comparison of the ischemic regions as predicted by the different APT quantification methods of a representative animal (Animal 1). Each plot corresponds to the comparison of a pair of quantification methods. The white region indicates overlap between the two ischemic masks; purple represents areas present only in the top legend method, and green represents areas present only in the left legend method. The Jaccard index *J* is displayed in the top left corner of each plot. *J* in the off-diagonal plots (white font) correspond to the comparison between each pair of quantification method; *J* in the diagonal plots (yellow font) correspond to comparison of the APT lesion and ADC lesion.

Figure 4. Pearson's correlation coefficients between the relative quantified MTR_{asym}, T_1-normalized MTR_{asym}, AREX, LDA, and multi-Lorentzian fitting. Each plot corresponds to the correlation between a pair of quantification methods; the correlation coefficient is shown in the top left corner of the plot, where red, green, blue, and black font indicated "very strong", "moderate", "weak", and "very weak" correlations respectively.

Supplementary Figure and Table Captions

Supplementary Figures

Supporting Figure S1. MR images of Animals 5 and 6 that were subject to MCAO. The first column shows the ADC images (μm^2/ms), overlaid with the ischemic (red) and contralateral (blue) regions of interest (ROI). The second and third column show the T_1 (s) and T_2 maps (ms); subsequent columns correspond to APT images generated using different quantification methods: MTR_{asym}, T_1-normalized MTR_{asym}, AREX, LDA, and multi-Lorentzian fitting (%). The final row shows the relative quantified APT effects of all six animals (n = 6) within the contralateral and ischemic tissues of each quantification method; * indicates a significant difference between the two tissues at 5% significance level.

Supporting Figure S2. ADC (μm^2/ms), CBF (mL/100g/min), and APT (%) images of Animals 5 and 6, with the respective ischemic areas outlined: ADC – white, CBF – green, and APT – blue. For every animal, the ADC and APT images are shown in the top row along with the binary ischemic area overlaps of all five APT methods in the last column, where higher intensity indicates a higher overlap. The bottom row shows the CBF map as well as the CBF/APT/ADC lesion mismatches of every APT quantification method; the display priority in the mismatch plots is white > blue > green.

Supporting Figure S3. ADC (μm^2/ms), T_1 (s), and T_2 (ms) maps and corresponding ischemic areas of the six animals. For each animal, the ADC lesion is shown in red line, overlaid on all images; T_1 and T_2 predicted ischemic lesions are shown in blue lines.

Supporting Figure S4. Average z-spectra within the ADC ischemic (red) and contralateral (blue) areas of Animals 1 – 6.

Supporting Figure S5. K-means clustering of the quantified APT effects of the different APT quantification methods. The quantified values were segmented into two clusters – ischemic tissue (red) and non-ischemic tissue (blue).

Supplementary Tables

Supporting Table S1. Summary of APT quantification methods for ischemic stroke imaging. The most commonly used methods based on literature are shown in bold font; quantification methods used in the present study are underlined. The white shaded entries are model-free methods; gray shaded entries are model-based methods.

Supporting Table S2(a) – (f). *P*-values of Mann-Whitney U test between the relative quantified effects (values) in the APT ischemic lesions of Animals 1 – 6 using the different quantification methods. Bold font indicates a significant difference ($P < 0.05$).

Supporting Table S3. Reported changes in quantified MTR_{asym}(~3.5 ppm) in ischemic stroke.

Supporting Table S4. Experimental parameters of the studies reporting MTR_{asym}(~3.5 ppm) results.

Figures

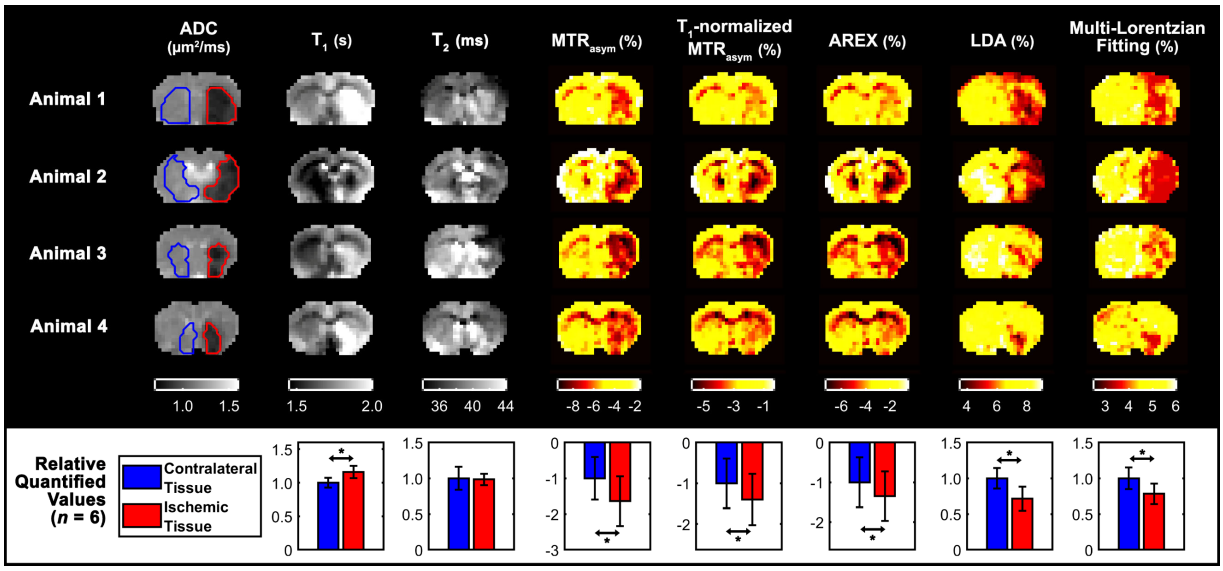

Figure 1. MR images of the four representative rats (Animals 1 – 4) subject to MCAO shown in the first four rows respectively. The first column shows the ADC images (μm^2/ms), overlaid with the ischemic (red) and contralateral (blue) regions of interest (ROI). The second and third column show the T_1 (s) and T_2 maps (ms); subsequent columns correspond to APT images generated using different quantification methods: MTR_{asym}, T_1-normalized MTR_{asym}, AREX, LDA, and multi-Lorentzian fitting (%). The final row shows the relative quantified APT effects of all six animals (n = 6) within the contralateral and ischemic tissues of each quantification method; * indicates a significant difference between the two tissues at 5% significance level.

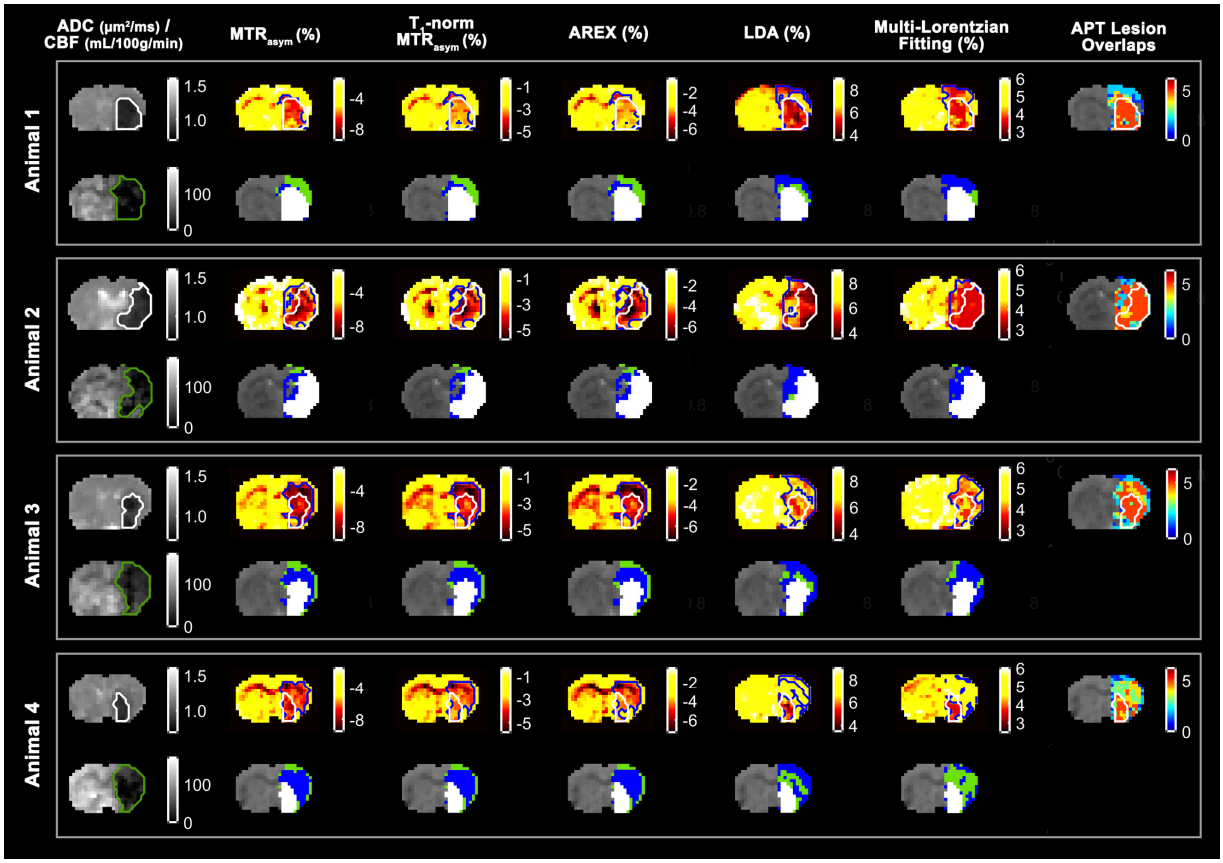

Figure 2. ADC (μm^2/ms), CBF (mL/100g/min), and APT (%) images of four representative animals (Animals 1 – 4), with the respective ischemic areas outlined: ADC – white, APT – blue and CBF – green. For every animal, the ADC and APT images are shown in the top row along with the binary ischemic area overlaps of all five APT methods in the last column, where higher intensity indicates a higher overlap. The bottom row shows the CBF map as well as the CBF/APT/ADC lesion mismatches of every APT quantification method; the display priority in the mismatch plots is white > blue > green.

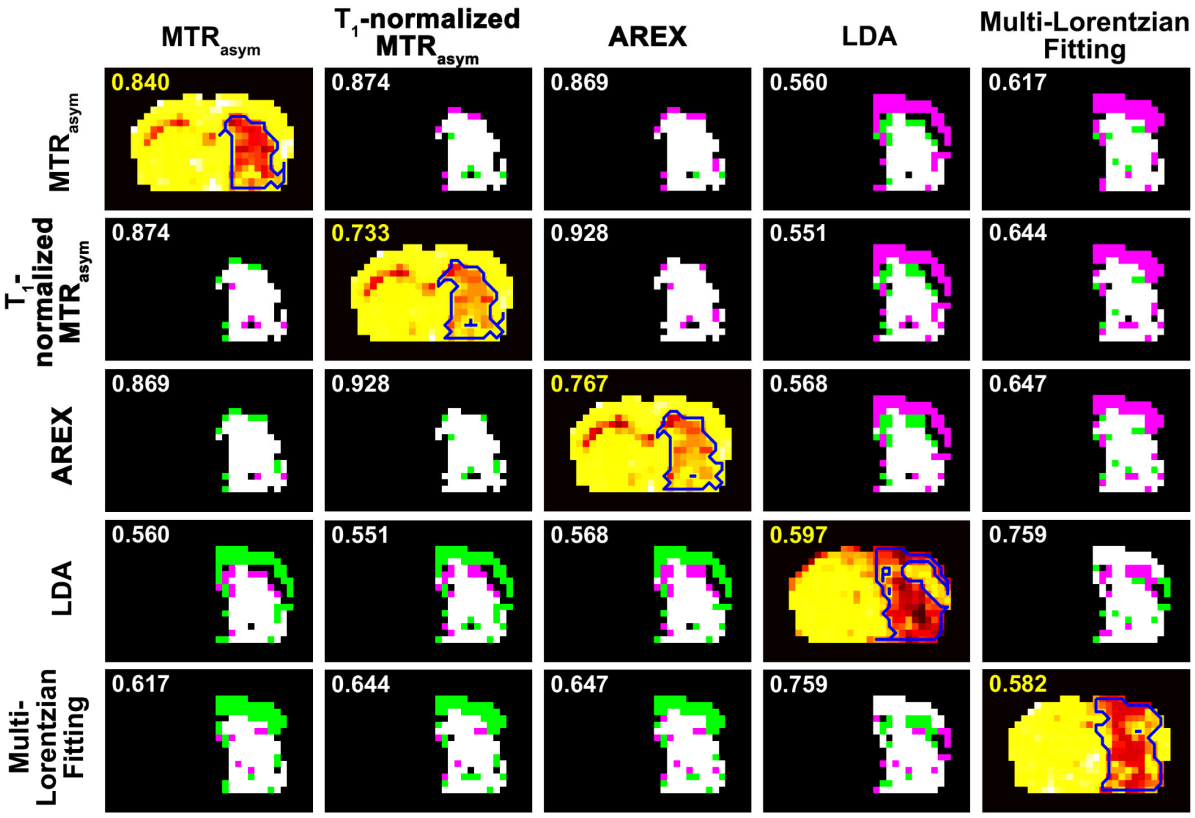

Figure 3. Comparison of the ischemic regions as predicted by the different APT quantification methods of a representative animal (Animal 1). Each plot corresponds to the comparison of a pair of quantification methods. The white region indicates overlap between the two ischemic masks; purple represents areas present only in the top legend method, and green represents areas present only in the left legend method. The Jaccard index J is displayed in the top left corner of each plot. J in the off-diagonal plots (white font) correspond to the comparison between each pair of quantification method; J in the diagonal plots (yellow font) correspond to comparison of the APT lesion and ADC lesion.

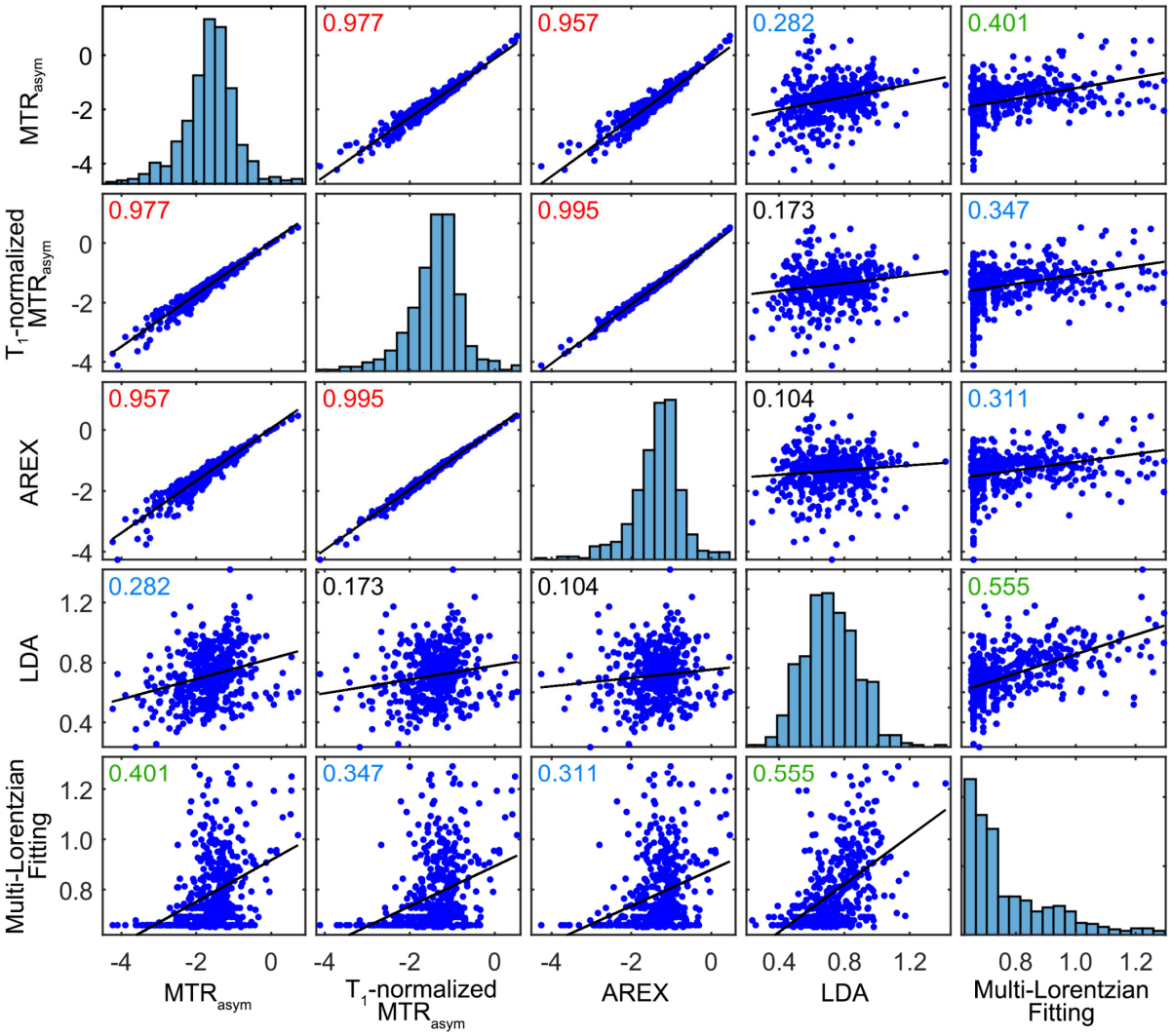

Figure 4. Pearson's correlation coefficients between the relative quantified MTR_{asym}, T_1-normalized MTR_{asym}, AREX, LDA, and multi-Lorentzian fitting. Each plot corresponds to the correlation between a pair of quantification methods; the correlation coefficient is shown in the top left corner of the plot, where red, green, blue, and black font indicated "very strong", "moderate", "weak", and "very weak" correlations respectively.